Electronic Supplementary Information

Intercalated Complexes of 1T'-MoS_2 Nanosheets with Alkylated Phenylenediamines as Excellent Catalysts for Electrochemical Hydrogen Evolution

In Hye Kwak,[a,†] Ik Seon Kwon,[a,†] Hafiz Ghulam Abbas,[b,†] Jaemin Seo,[a] Gabin Jung,[a]
Yeron Lee,[a] Jaemin Seo,[a] Doyeon Kim, [a] Jae-Pyoung Ahn,[c] Jeunghee Park,[a,]*
and Hong Seok Kang[d,]*

[a] Department of Chemistry, Korea University, Sejong 339-700, Republic of Korea; *E-mail address: parkjh@korea.ac.kr (J. Park)

[b] Department of Nanoscience and Nanotechnology, Jeonbuk National University, Chonju, Chonbuk 560-756, Republic of Korea.

[c]Advanced Analysis Center, Korea Institute of Science and Technology, Seoul 136-791, Republic of Korea.

[d] Department of Nano and Advanced Materials, College of Engineering, Jeonju University, Chonju, Chonbuk 55069, Republic of Korea; *E-mail address: hsk@jj.ac.kr

[†] I. H. Kwak, I. S. Kwon, and H. G. Abbas equally contribute as the first author.

Contents

Table S5. Various parameters of intercalated (4×4) $MoS_{2-2x}N_x$ (x = 12.5%) supercell in the 1T' phase.

III. Supplementary Figures

Fig. S1 TEM images of MS-0, MS-PPD, and MS-DMPD.

Fig. S2 XRD data.

Fig. S3 XANES spectra.

Fig. S4 Raman spectra.

Fig. S5 XPS survey and fine-scanned S 2p peaks.

Fig. S6 NMR spectra.

Fig. S7 Fine-scanned N 1s peak region.

Fig. S8 Chronoamperometric and chronopotentiometric responses.

Fig. S9 Nyquist plots.

Fig. S10 Cyclic voltammograms (CV) for evaluation of double-layer capacitance.

Fig. S11 Structures of five different configurations of $MoS_{2-2x}N_x$ (x = 12.5%).

Fig. S12 $\Delta q(z)$ and $\Delta Q(z)$ versus z of (4×4) MoS_2-PD at [PD] = 12.5%.

Fig. S13 TDOS of (4×4) MoS_2-PPD and (4×4) MoS_2-TMPD.

Fig. S14 Projected DOS (PDOS) of (a) (4×4) MoS_2-PPD and (b) MoS_2-TMPD.

I. Experimental Section

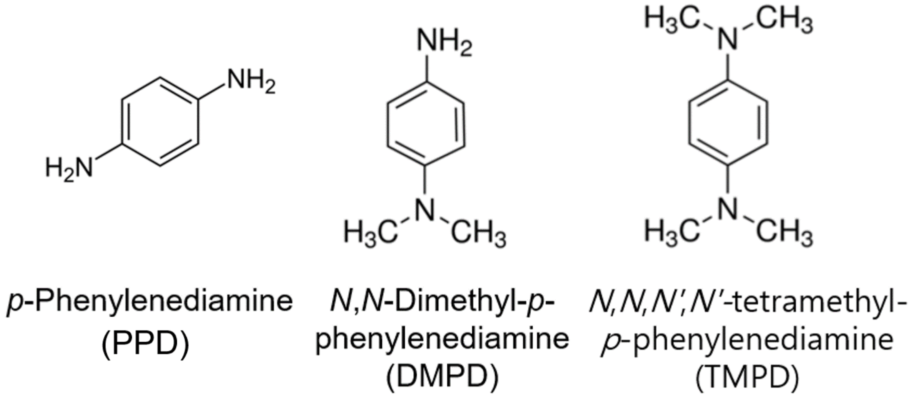

Scheme S1. Structures of alkylated phenylenediamine molecules as intercalants, which are referred to as PPD, DMPD, and TMPD.

The structures of PDs are shown in Scheme S1.

Characterization. The products were characterized by field-emission transmission electron microscopy (FE TEM, FEI TECNAI G2 200 kV, Jeol JEM 2100F, HVEM). Energy-dispersive X-ray fluorescence spectroscopy (EDX) with elemental maps was measured using a TEM (FEI Talos F200X) operated at 200 kV that equipped with high-brightness Schottky field emission electron source (X-FEG) and Super-X EDS detector system (Bruker Super-X). This EDX has powerful sensitivity and resolution in the low photon energy region. Fast Fourier-transform (FFT) images were generated by the inversion of the TEM images using Digital Micrograph GMS1.4 software (Gatan Inc.). High-resolution X-ray diffraction (XRD) patterns were obtained using the 9B and 3D beamlines of the Pohang Light Source (PLS) with monochromatic radiation ($\lambda = 1.54595$ Å). XRD pattern measurements were also carried out in a Rigaku D/MAX-2500 V/PC using Cu K_α radiation ($\lambda = 1.54056$ Å). X-ray photoelectron spectroscopy (XPS) measurements were performed using the 8A1 beam line of the PLS, as well as a laboratory-based spectrometer (Thermo Scientific Theta Probe) using a photon energy of 1486.6 eV (Al Kα). X-ray absorption near edge spectra (XANES) and extended X-ray absorption fine structure (EXAFS) spectra at the Mo K-edge were collected in transmission mode using the 10C beam line of the PLS with a ring current of 350 mA at 3.0 GeV. Energy calibration was carried out by simultaneously measuring the reference spectrum of Mo metal foil. Least-squares fits of EXAFS data were performed using the Athena and Artemis software packages, version 0.9.25.

The solid-state ^{13}C (100.64 MHz) NMR spectra were acquired on a Bruker AVANCE II^{+} 400 MHz NMR system (at the KBSI Seoul Western Center) equipped with a Bruker 3.2 mm bore HXY probe operating in HX mode. The magic angle spinning ^{13}C NMR experiments (one pulse method) were performed using a pulse length of 2 μs for a π/2 pulse length of 5 μs, and a pulse repetition delay time of 3 s. The spectra were referenced to an external adamantane standard in which the peak at higher chemical shift was set at 38.43 ppm. The spectra were processed using the Bruker Topspin software (version 3.2) using conventional techniques, and a 50 Hz line broadening window function was applied in all cases.

Electrochemical Measurements. HER electrocatalysis (in 0.5 M H_2SO_4 electrolyte) was measured using a linear sweeping from 0 to -0.8 V (vs. RHE) with a scan rate of 2 mV s^{-1}. A saturated calomel electrode (SCE, KCl saturated, Basi Model RE-2BP) was used as reference electrode, and a graphite rod (6 mm dia. × 102 mm long, 99.9995%, Alfa Aesar) was used as counter electrode. The electrolyte was purged with H_2 (ultrahigh grade purity) during the measurement. The applied potentials (E) reported in our work were referenced to the reversible hydrogen electrode (RHE) through standard calibration. In 0.5 M H_2SO_4 electrolyte (pH 0), E (vs. RHE) = E (vs. SCE) + E_{SCE} (= 0.241 V) + 0.0592 pH = E (vs. SCE) + 0.241 V. The overpotential (η) was defined as E (vs. RHE). 4 mg MS sample was mixed with 1 mg carbon black (Vulcan XC-72) dispersed in Nafion (20 μL) and isopropyl alcohol (0.98 mL). The catalyst materials (0.39 mg cm^{-2}) were deposited on a glassy carbon rotating disk electrode (RDE, area = 0.1641 cm^2, Pine Instrument),), and a rotation speed of 1600 rpm was used for the linear sweep voltammetry (LSV) measurements. The Pt/C (20 wt.% Pt in Vulcan carbon black, Sigma-Aldrich) tested as reference sample using the same procedure.

Electrochemical impedance spectroscopy (EIS) measurements were carried out for the electrode in an electrolyte by applying an AC voltage of 10 mV in the frequency range of 100 kHz to 0.1 Hz at a bias voltage of -0.15 V (vs. RHE). To measure double-layer capacitance via CV, a potential range in which no apparent Faradaic processes occur was determined from static CV. This range is 0.1–0.2 V. All measured current in this non-Faradaic potential region is assumed to be due to double-layer capacitance. The charging current, i_c, is then measured from CVs at multiple scan rates. The working electrode was held at each potential vertex for 10 s before beginning the next sweep. The charging current density (i_c) is equal to the product of the scan rate (ν) and the electrochemical double-layer capacitance (C_{dl}), as given by equation $i_c = \nu\, C_{dl}$. The difference ($\Delta J_{0.15}$) between the anodic charging and cathodic discharging currents measured at 0.15 V (vs. RHE) was used for i_c. Thus, a plot of $\Delta J_{0.15}$ as a function of ν yields a straight line with a slope equal to $2 \times C_{dl}$. The scan rates were 20–100 mV s^{-1}.

TOF Calculation. The active site density and per-site turnover frequency (TOF) have been estimated as follows. It should be emphasized that since the nature of the active sites of the catalyst is not clearly understood yet and the real surface area for the nanostructured heterogeneous catalyst is hard to accurately determine, the following result is really just an estimation. Two methods were used to calculate the active site density.

Method 1. To estimate the active surface site density, we used the C_{dl} value, and further calculate the electrochemically active surface area. The roughness factor of MS-TMPD (basically the surface area ratio between the catalyst vs. the metal electrodes (0.035 mF cm^{-2}), [S1] for example, is 47.2 mF cm^{-2}/0.035 mF cm^{-2} = 1349.

The number of catalytic sites on the surface of flat catalyst can be calculated based on the crystal structure of distorted octahedral-phase 1T' MoS_2. Using the lattice parameters of 1T' phase MoS_2 (we calculated as a = 3.18 Å, b = 3.26 Å, γ = 119°) and assuming one active site per MoS_2 (which translates into on reactive sites per unit cell), the density of surface active sites is: $1/(0.5 \times 3.18 \times 3.26 \times \sin 119°) \times 10^{16}$ cm^{-2} = 2.2×10^{15} atom cm^{-2}).[S2] Our DFT calculation shows that the N atoms (10%) are most active sites, so the number of surface active sites is calculated as $0.1 \times 2.2 \times 10^{15}$ atom cm^{-2} = 2.2×10^{14} atom cm^{-2}. The density of surface active sites (m) of MS-TMPD on geometric area: 2.2×10^{14} atom cm^{-2} × 1349 (= roughness factor) = 3.0×10^{17} atom cm^{-2}.

The total number of hydrogen (H_2) gas turns overs was calculated from the current density (J in mA cm^{-2}) according to n_{H2} = J (mA cm^{-2})/1000 mA × 1 C s^{-1} × 1 mol e^-/96486 C × (1 mol H_2/2 mol e^{-1}) × (6.022×10^{23} H_2 molecules/1 mol H_2) = 3.12×10^{15} H_2 s^{-1} cm^{-2} per mA cm^{-2}.

For MS-TMPD, the per-site TOF at η = 0.2 V (with a current density of 350 mA cm^{-2}) is n_{H2}/m (=density of surface active sites) = $350 \times 3.12 \times 10^{15}$ H_2 s^{-1} cm^{-2} / 3.0×10^{17} atom cm^{-2} = 3.6 H_2 s^{-1}. In the case of MS-0, MS-PPD and MS-DMPD, the TOF was estimated as 0.084, 0.28 and 1.2 s^{-1}, respectively.

Method 2.[S3]

The active sites are determined by calculating cathodic charge (Q_C) from the CV curves (as shown below), which was obtained in 0.1 M phosphate buffer solution (pH: 7, Range = -0.2 ~ 0.6 V vs. RHE). While it is difficult to assign the observed peaks to a given redox couple, the integrated charge over the whole potential range should be proportional to the total number of active sites.

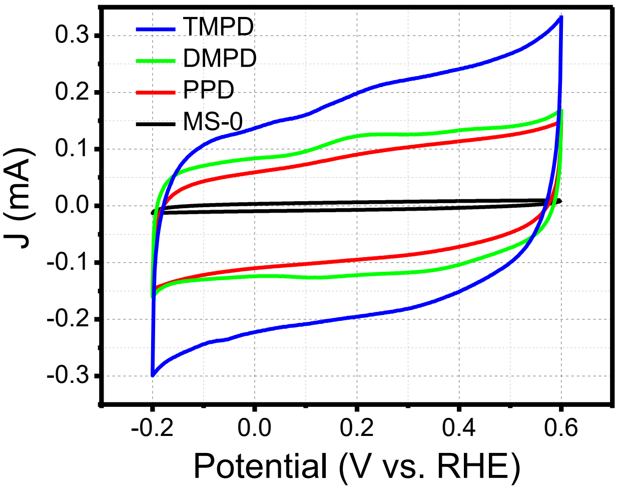

The formula employed to find the number of active sites is given by $m = \frac{Q_C}{2F}$. Here, m is the number of active sites in moles, Q_C is cathodic charge in Coulomb and the factor ½ is number of electrons taking part in oxidation/reduction process. The per-site TOF (= n_{H2} / m) for MS-TMPD was calculated as 50 s^{-1} at 0.2 V. In the case of MS-0, MS-PPD and MS-DMPD, the TOF was estimated as 0.66, 5.7, and 22 s^{-1}, respectively.

We summarized the TOF values using two methods.

Guest	J (mA cm^{-2}) at 0.2 V	n_{H2}	Method 1			Method 2		
			Roughness factor	m	TOF	Q (mC)	m	TOF
None	0.170	5.3×10^{14}	288.6	6.3×10^{16}	0.084	0.256	8.0×10^{14}	0.66
PPD	20.3	6.3×10^{16}	1009	2.2×10^{17}	0.28	3.524	1.1×10^{16}	5.7
DMPD	98.2	3.1×10^{17}	1186	2.6×10^{17}	1.2	4.380	1.4×10^{16}	22
TMPD	350	1.1×10^{18}	1349	3.0×10^{17}	3.7	7.172	2.2×10^{16}	50

References:

(S1) C. C. L. McCrory, S. Jung, I. M. Ferrer, S. M. Chatman, J. C. Peters and T. F. Jaramillo, *J. Am. Chem. Soc.*, 2015, **137**, 4347-4357.

(S2) Y. Yin, J. Han, Y. Zhang, X. Zhang, P. Xu, Q. Yuan, L. Samad, X. Wang, Y. Wang, Z. Zhang, P. Zhang, X. Cao, B. Song and S. Jin, *J. Am. Chem. Soc.*, 2016, **138**, 7965-7972.

(S3) M. A. R. Anjum, H. Y. Jeong, M. H. Lee, H. S. Shin and J. S. Lee, *Adv. Mater.*, 2018, **30**, 1707105.

II. Supplementary Tables

Table S1. Fitting parameters of EXAFS data (**Fig. 2b**) for the MoS_2 samples.

Sample	Scattering Path	R (Å)[a]	CN[b]	ΔE (eV)[c]	σ^2 (Å^2)[d]
MS-0	Mo-S	2.40	6.2 ± 0.3	1.3	0.0028
	Mo-Mo	3.16	4.2 ± 0.8	0.8	0.0036
MS-PPD	Mo-S	2.40	3.9 ± 0.5	-1.1	0.0074
	Mo-Mo	2.75	1.4 ± 0.8	2.7	0.0085
MS-DMPD	Mo-S	2.40	4.5 ± 0.6	-2.1	0.0082
	Mo-Mo	2.76	1.8 ± 1.2	1.2	0.0111
MS-TMPD	Mo-S	2.39	3.6 ± 0.7	-2.8	0.0076
	Mo-Mo	2.75	1.7 ± 1.5	1.3	0.0110

[a] Distance between scattering atoms.

[b] Coordination number of Mo atoms.

[c] Edge energy shift, representing between the energy grids of experimental and theoretical data.

[d] Debye-Waller factor, which measure the static and thermal disorder, is three-times larger for the intercalated MS samples than MS-0. It suggests that the intercalation produces a broad range of Mo-S and Mo-Mo distances.

Table S2. Impedance parameters for the equivalent circuit that was shown in **Fig. S9**, and the double-layer capacitance (C_{dl}) as shown in **Fig. S10**.

`	EIS		C_{dl} (mF cm^{-2})
Samples	R_s (Ω)	R_{ct} (Ω)	
MS-0	6.4	850.2	10.1
MS-PPD	5.6	75.1	35.3
MS-DMPD	5.7	24.1	41.6
MS-TMPD	6.0	15.6	47.2

Table S3. Comparison of HER performance (in pH 0) of 1T or 1T′ phase MoS_2 in the literatures.

Reference	Materials	Phase	$E_{J=10}$ (mV) at 10 mA cm^{-2}	Tafel slope (mV dec^{-1})
S1	Multiphasic MoS_2	1T	234	46
S2	MoS_2 monolayer	1T'	300	83
S3	TBA-MoS_2	1T	~340	102
S4	Li-MoS_2 QDs	1T	92	44
S5	Functionalized MoS_2 nanosheet	1T	348	75
S6	MoS_2 Crystals	1T'	~200	100
S7	MoS_2/graphene	1T	137	48
S8	Alkali metal MoS_2	1T	240	48
S9	MoS_2 nanodot	1T	173	53
S10	Pd-MoS_2	1T	78	62
Present work	TMPD-intercalated MoS_2	1T'	153	35

References:

(S1) D. Wang, X. Zhang, S. Bao, Z. Zhang, H. Fei and Z. Wu, *J. Mater. Chem. A*, 2017, **5**, 2681-2688.

(S2) J. Zhang, J. Wu, H. Guo, W. Chen, J. Yuan, U. Martinez, G. Gupta, A. Mohite, P. M. Ajayan and J. Lou, *Adv. Mater.*, 2017, **29**, 1701955.

(S3) S. Presolski, L. Wang, A. H. Loo, A. Ambrosi, P. Lazar, V. Ranc, M. Otyepka, R. Zboril, O. Tomanec, J. Ugolotti, Z. Sofer and M. Pumera, *Chem. Mater.*, 2017, **29**, 2066-2073.

(S4) W. Chen, J. Gu, Q. Liu, R. Luo, L. Yao, B. Sun, W. Zhang, H. Su, B. Chen, P. Liu and D. Zhang, *ACS Nano*, 2018, **12**, 308-316.

(S5) E. E. Benson, H. Zhang, S. A. Schuman, S. U. Nanayakkara, N. D. Bronstein, S. Ferrere, J. L. Blackburn and E. M. Miller, *J. Am. Chem. Soc.*, 2018, **140**, 441-450.

(S6) Y. Yu, G. H. Nam, Q. He, X. J. Xu, K. Zhang, Z. Yang, J. Chen, Q. Ma, M. Zhao, Z. Liu, F. R. Ran, X. Wang, H. Li, X. Huang, B. Li, Q. Xiong, Q. Zhang, Z. Liu, L. Gu, Y. Du, W. Huang and H. Zhang, *Nat. Chem.*, 2018, **10**, 638-643.

(S7) P. Xiong, R. Ma, N. Sakai, L. Nurdiwijayanto and T. Sasaki, *ACS Energy Lett.*, 2018, **3**, 997-1005.

(S8) J. Luxa, P. Vosecký, V. Mazánek, D. Sedmidubský, M. Pumera and Z. Sofer, *ACS Catal.*, 2018, **8**, 2774-2781.

(S9) C. Tan, Z, Luo, A. Chaturvedi, Y. Cai, Y. Du, Y. Gong, Y. Huang, Z. Lai, X. Zhang, L. Zheng, X. Qi, M. H. Goh, J. Wang, S. Han, X. J. Wu, L. Gu, C. Kloc and H. Zhang, *Adv. Mater.*, 2018, **30**, 1705509.

(S10) Z. Luo, Y. Ouyang, H. Zhang, M. Xiao, J. Ge, Z. Jiang, J. Wang, D. Tang, X. Cao, C. Liu and W. Xing, *Nat. Commun.*, 2018, **9**, 2120.

Table S4. Comparison of H_2 evolution turnover frequency (TOF) of MoS_2 (in pH 0) in the literatures.

Reference	**Materials**	**TOF (H_2 s^{-1})**
S1	Defect-rich MoS_2	0.725 at 0.3 V
S2	Single layer MoS_2	0.019-0.046 at 0 V
S3	S depleted MoS_2	8.74 at 0.2 V
S4	1T' monolayer MoS_2	3.8 ± 1.6 at 0.077 V
S5	1T/2H MoS_2	~ 0.15 at 0.2 V
S6	Vacancy rich surface MoS_2	~9 at 0.2 V
S7	Pd-MoS_2	16.54 at 0.2 V
Present work	TMPD-intercalated MoS_2	3.7 at 0.2 V

References:

(S1) J. Xie, H. Zhang, S. Li, R. Wang, X. Sun, M. Zhou, J. Zhou, X. W. Lou and Y. Xie, *Adv. Mater.*, 2013, **25**, 5807-5813.

(S2) D. Voiry, R. Fullon, J. Yang, C. C. C. Silva, R. Kappera, I. Bozkurt, D. Kaplan, M. J. Lagos, P. E. Batson, G. Gupta, A. D. Mohite, L. Dong, D. Er, V. B. Shenoy, T. Asefa and M. Chhowalla, *Nat. Mater.*, 2016, **15**, 1003-1009.

(S3) L. Lin, N. Miao, Y. Wen, S. Zhang, P. Ghosez, Z. Sun and D. A. Allwood, *ACS Nano*, 2016, **10**, 8929-8937.

(S4) J. Zhang, J. Wu, H. Guo, W. Chen, J. Yuan, U. Martinez, G. Gupta, A. Mohite, P. M. Ajayan and J. Lou, *Adv. Mater.*, 2017, **29**, 1701955.

(S5) D. Wang, X. Zhang, S. Bao, Z. Zhang, H. Fei and Z. Wu, *J. Mater. Chem. A*, 2017, **5**, 2681-2688.

(S6) C. Tsai, H. Li, S. Park, J. Park, H. S. Han, J. K. Nørskov, X. Zheng and F. Abild-Pedersen, *Nat. Commun.*, 2017, **8**, 15113.

(S7) Z. Luo, Y. Ouyang, H. Zhang, M. Xiao, J. Ge, Z. Jiang, J. Wang, D. Tang, X. Cao, C. Liu and W. Xing, *Nat. Commun.*, 2018, **9**, 2120.

Table S5. Parameters of 2H-MoS_2 and PD-intercalated (4×4) $MoS_{2-2x}N_x$ (x = 0.125) in the 1T' phase with R_0', R_1', and A configurations.

PD	[PD] (%)	Configuration	a, b, c (Å) α, β, γ (°)^a	E_{rel} (eV)^b	E_{ic} (eV)^c	ΔQ (e)^d	ℓ_{Mo-Mo} (Å)^e	ℓ_{Mo-S} (Å)^e	ℓ_{Mo-N} (Å)^e
None	0		12.64, 12.64, 12.53 90.0, 90.0, 120°	--	--	--	3.16	2.40	--
PPD	6.25	R_0'	12.94, 13.00, 18.34 90.0, 90.0, 119.0	0.00	-0.12	0.40	2.78 (2.67, 2.68, 2.74, 2.76, 2.91, 2.93)	2.38 (2.32, 2.35, 2.39, 2.40, 2.41, 2.42)	1.98 (1.95, 1.99, 2.00)
		R_1'	12.60, 12.67, 18.33 90.0, 90.0, 119.0	0.96	0.36	-	2.92 (2.76, 2.78, 2.96, 2.98, 3.01, 3.04)	2.41 (2.36, 2.38, 2.39, 2.40, 2.44, 2.48)	2.04 (1.88, 2.01, 2.25)
		A	12.61, 12.84, 17.50 90.0, 90.0, 119.0	2.16	0.95	-	2.95 (2.80, 2.93, 2.95, 2.97, 3.03, 3.07)	2.42 (2.35, 2.38, 2.39, 2.40, 2.49, 2.53)	2.03 (1.86, 2.03, 2.22)
DMPD		R_0'	12.94, 13.01, 18.81 90.0, 90.0, 119.0	0.00	-0.30	0.73	2.74 (2.67, 2.69, 2.70, 2.74, 2.77, 2.89)	2.39 (2.36, 2.37, 2.38, 2.39, 2.42, 2.43)	1.98 (2.00, 1.96, 1.98)
		R_1'	12.61, 12.66, 19.01 90.0, 90.0, 119.0	0.26	-0.16	-	2.92 (2.75, 2.77, 2.96, 2.97, 3.01, 3.06)	2.42 (2.34, 2.39, 2.40, 2.42, 2.45, 2.50)	2.03 (1.89, 2.01, 2.20)
		A	12.61, 12.84, 18.93 90.0, 90.0, 119.0	1.44	0.43	-	2.93 (2.80, 2.78, 2.92, 2.96, 3.03, 3.09)	2.40 (2.36, 2.38, 2.39, 2.40, 2.44, 2.49)	2.05 (1.84, 2.04, 2.28)
TMPD		R_0'	12.93, 13.02, 18.75 90.0, 90.0, 119.0	0.00	-0.74	0.84	2.75 (2.68, 2.70, 2.74, 2.75, 2.78, 2.90)	2.37 (2.30, 2.35, 2.37, 2.38, 2.40, 2.42)	1.98 (1.97, 1.97, 2.00)
		R'_1	12.61, 12.66, 19.59 90.0, 90.0, 119.0	0.90	-0.29	-	2.91 (2.74, 2.77, 2.93, 2.98, 3.01, 3.05)	2.39 (2.36, 2.38, 2.39, 2.40, 2.41,2.43)	2.04 (1.88, 2.02, 2.22)
		A	12.60, 12.83, 19.44 90.0, 90.0, 119.0	2.16	0.34	-	2.88 (2.77, 2.81, 2.87, 2.92, 2.95, 3.00)	2.42 (2.33, 2.38, 2.40, 2.43, 2.45, 2.50)	2.04 (1.85, 2.05, 2.23)
PPD	12.5	R_0'	12.73, 12.95, 19.32 90.0, 90.0, 119.0	0.00	-0.14	0.26	2.78 (2.67, 2.69, 2.74, 2.76, 2.91, 2.93)	2.38 (2.32, 2.35, 2.39, 2.40, 2.41, 2.42)	1.98 (1.95, 1.99, 1.99)
		R_1'	12.67, 12.78, 19.32 90.0, 90.0, 119.0	0.06	-0.13	-	2.91 (2.75, 2.78, 2.84, 2.98, 3.05, 3,09)	2.39 (2.35, 2.37, 2.39, 2.40, 2.42, 2.43)	2.05 (1.89, 2.02, 2.25)
		A	12.63, 12.87, 18.87 90.0, 90.0, 119.0	0.09	-0.11	-	2.92 (2.81, 2.85, 2.92, 2.95, 2.98, 3.02)	2.39 (2.35, 2.37, 2.39, 2.40, 2.41, 2.43)	2.06 (1.83, 2.07, 2.29)
DMPD		R_0'	12.92, 13.03, 19.43 90.0, 90.0, 119.0	0.00	-0.68	0.52	2.74 (2.67, 2.69, 2.70, 2.74, 2.77, 2.89)	2.39 (2.36, 2.37, 2.38, 2.39, 2.42, 2.43)	1.98 (2.00,1.96,1.98)
		R_1'	12.67, 12.78, 19.40 90.0, 90.0, 119.0	0.22	-0.62	-	2.91 (2.78, 2.79, 2.85, 2.96, 3.03, 3.06)	2.38 (2.31, 2.38, 2.39, 2.40, 2.42, 2.43)	2.04 (1.88,2.01,2.23)
		A	12.73, 12.95, 19.30 90.0, 90.0, 119.0	0.63	-0.52	-	2.88 (2.79, 2.80, 2.82, 2.94, 2.98, 3.00)	2.37 (2.35, 2.36, 2.37, 2.38, 2.40, 2.41)	2.06 (1.83, 2.07, 2.30)
TMPD		R_0'	12.95, 13.05 19.37 90.0, 90.0, 119.0	0.00	-1.07	0.63	2.75 (2.68, 2.70, 2.74, 2.75, 2.78, 2.90)	2.37 (2.30, 2.35, 2.37, 2.38, 2.40, 2.42)	1.98 (1.97, 1.97, 2.00)

		R_1'	12.63, 12.68, 19.72 90.0, 90.0, 119.0	0.67	-0.88	-	2.90 (2.75, 2.76, 2.94, 2.96, 2.99, 3.03)	2.39 (2.36, 2.37, 2.39, 2.40, 2.41, 2.42)	2.04 (1.89, 2.02, 2.23
		A	12.73, 12.95, 19.40 90.0, 90.0, 119.0	1.81	-0.60	-	2.88 (2.79, 2.80, 2.82, 2.94, 2.98, 3.00)	2.37 (2.35, 2.36, 2.37, 2.38, 2.40, 2.41)	2.06 (1.83, 2.07, 2.30)

[a] Optimized lattice parameters of each configuration. In configuration R_0', $a = 3.23$ Å, $b = 3.25$ Å, $c = 19$ Å on average. The angle between the a and b axes is 119°. The lattice constants of non-intercalated 1T′ phase were calculated as $a = 3.18$ Å, $b = 3.26$ Å, $c = 12.16$ Å by our group.[S1] The lattice constant b is close to the experimental value ($a = 3.26$ Å) that was obtained by XRD (see **Fig. S2**).

[b] Relative energy with respect to the most stable configuration. Three different configurations were investigated for the distribution of S vacancies, which are referred to as A, R_0', and R_1' in stability order of 1T′ MoS_2 with no PD intercalation. The R_0' and R_1' are significantly more stable than the R_0 and R_1 that shown in our previous work, respectively.[S2] **Fig. S11**shows that they are slightly different from old ones in vacancy distributions. In configuration R_0', each of four MoS_2 sublayers contains two consecutive S vacancies, one half of them being filled with N atoms. On the other hand, vacancies are randomly scattered in a non-contiguous way in configuration A. After the PD-intercalation, R_0' becomes the most stable, while A gets the least stable. Therefore, we focused on R_0' for further calculations

[c] Intercalation energy per molecule.

[d] Total charge transfer from a PD molecule to MoS_2 layers: it is defined as $\Delta Q = Q_{\mathrm{max}} - Q_{\mathrm{min}}$, where Q_{max} and Q_{min} correspond to the adjacent maximum and minimum of $Q(z)$ at $z = z_{\mathrm{max}}$ and z_{min}, respectively (see **Fig. S12**).[S1]

[e] The average distance between two atoms, which was obtained from values in the parenthesis. The first two values represent the Mo-Mo distances along the alternating direction, while the last one denotes the average distance along the direction which is oriented at 60° with respect to the first one in the same plane.

References:

(S1) I. S. Kwon, I. H. Kwak, H. G. Abbas, G. Jung, Y. Lee, J. Park, S. J. Yoo, J. G. Kim and H. S. Kang, *Nanoscale*, 2018, **10**, 11349-11356

(S2) I. H. Kwak, I. S. Kwon, H. G. Abbas, G. Jung, Y. Lee, T. T. Debela, S. J. Yoo, J. G. Kim, J. Park and H. S. Kang, *Nanoscale*, 2018, **10**, 14726-14735.

III. Supporting Figures

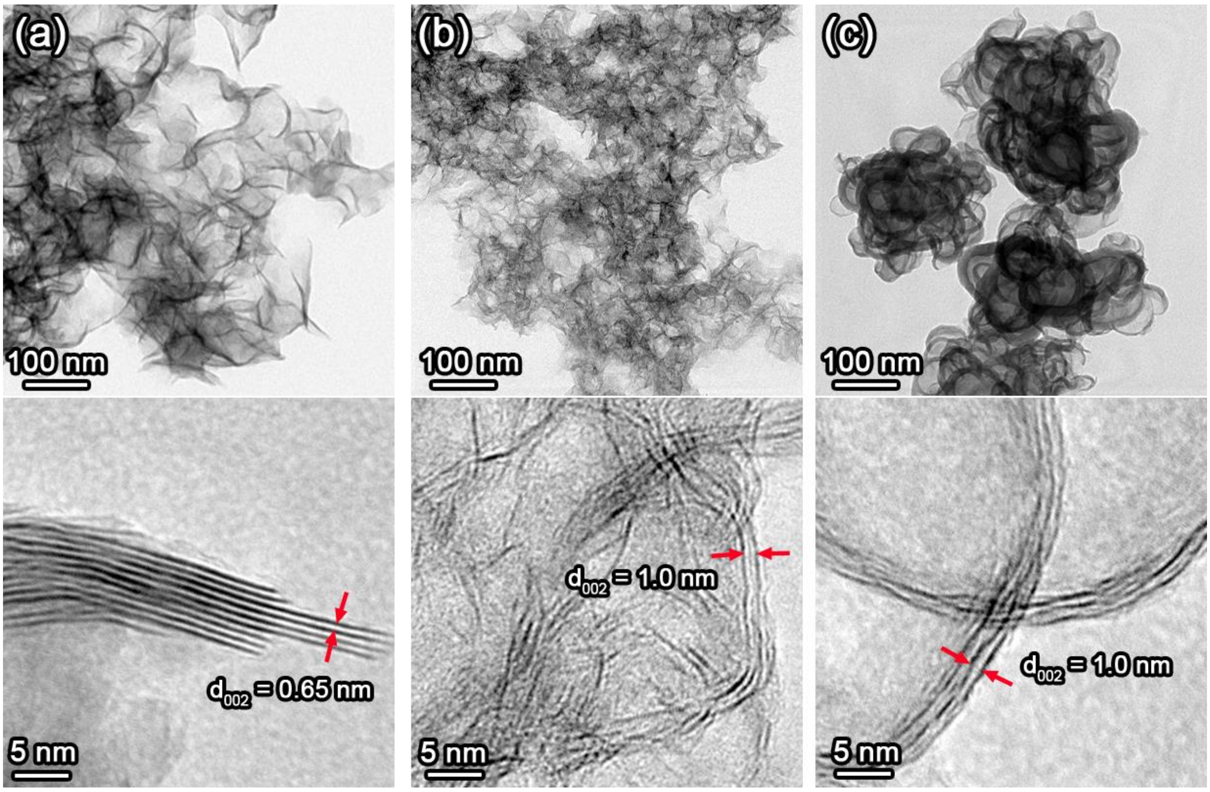

Fig. S1 HRTEM image of (a) MS-0, (b) MS-PPD, and (c) MS-DMPD. The MS-DMPD exhibit the similar nanofoam structures as that of MS-TMPD. The MS-0 consisted of the flower-like MoS_2 nanosheets. The morphology of MS-PPD is rather closer to that of MS-DMPD than that of MS-0. The lattice-resolved TEM image shows that the average distance between adjacent MoS_2 layers (d_{002}) is 6.5, 10, 10 Å, for MS-0, MS-PPD, and MS-DMPD, respectively.

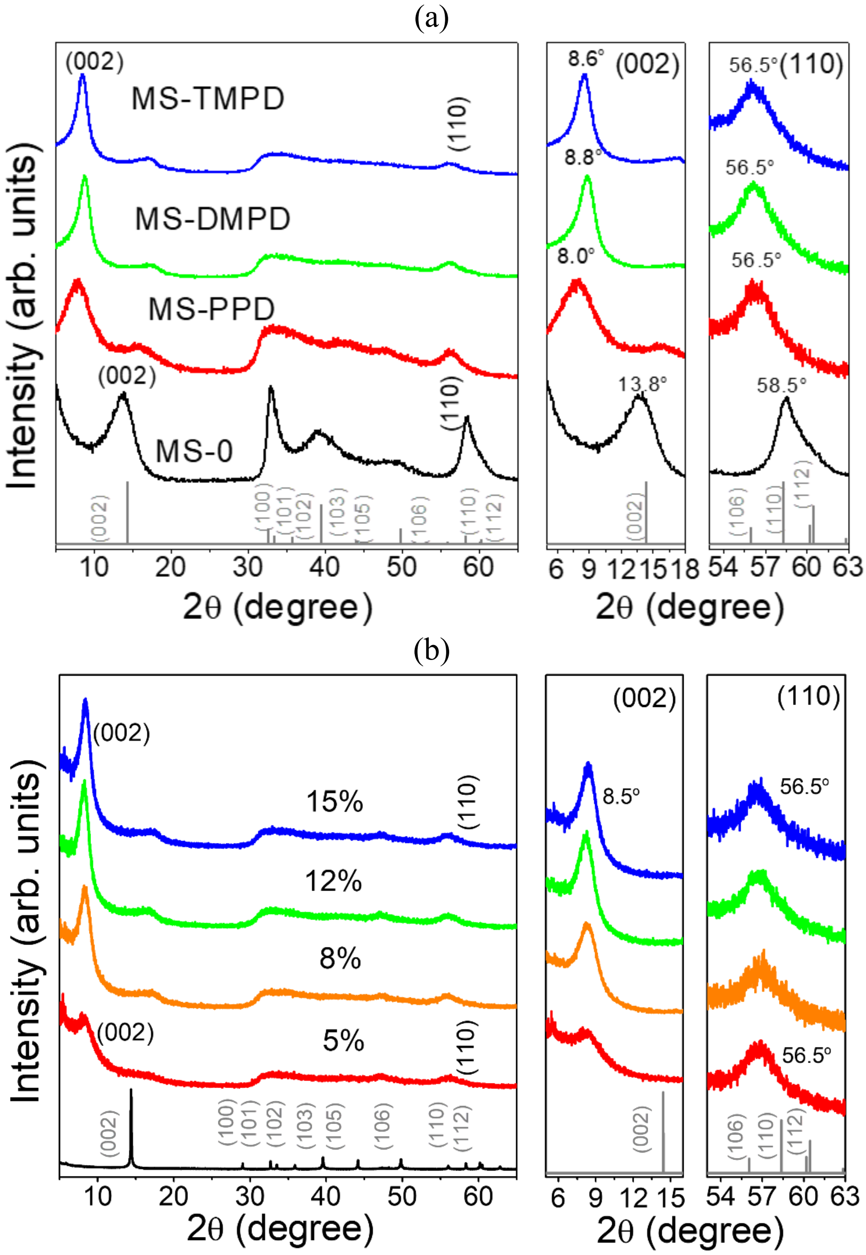

Fig. S2 XRD patterns of (a) MS-0, MS-PPD, MS-DMPD, and MS-TMPD (with 8% intercalants); (b) MS-TMPD with 5%, 8%, 12%, and 15% intercalated TMPD. The peaks were referenced to those of the 2H phase MoS$_2$ (JCPDS No. 87-2416; a = 3.160 Å and c = 12.290 Å). We observed that the (002) peaks of the intercalated MoS$_2$ are shifted to 2θ = 8.0-8.8°, for all PD molecules in the range of 5-19%. The intercalation of PDs leads to a significant increase in the corresponding c = 20 Å. The 2θ position of (110) peak is 56.5°, corresponding to the lattice constant a (or b) = 3.27 Å of 1T′ phase MoS$_2$

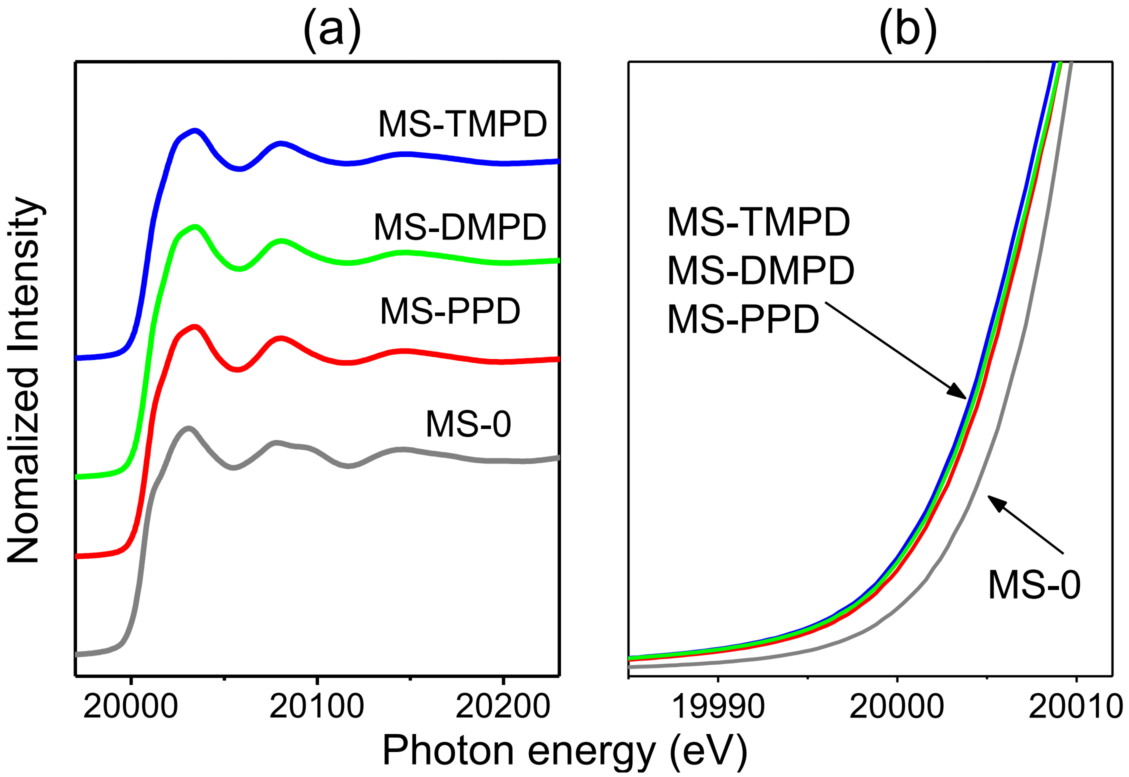

Fig. S3 (a) XANES spectra at the Mo K edge for MS-0, MS-PPD, MS-DMPD, and MS-TMPD and (b) magnified scaled spectrum in the edge.

The evolution of the local crystal structure of MoS_2 upon the intercalation of aromatic amines was probed with Mo K-edge X-ray absorption near edge spectra (XANES) analysis. The edge energies of all intercalated MoS_2 are lower than those of MS-0. It suggests that the intercalation induces more metallic properties of Mo.

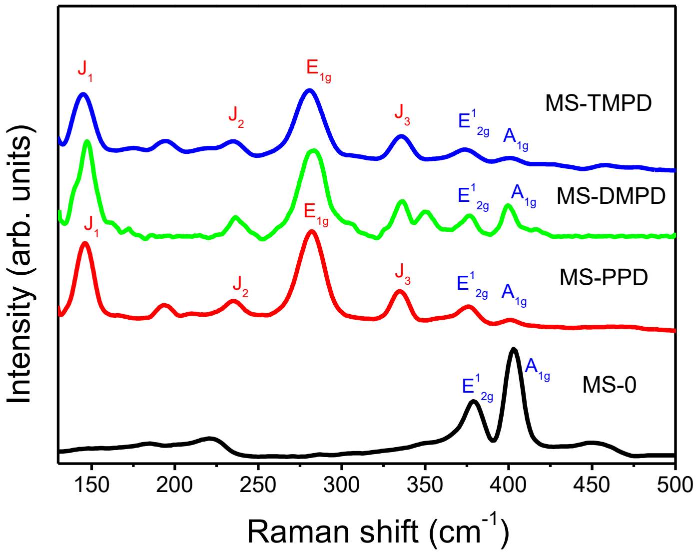

Fig. S4 Raman spectrum of the samples. Excitation laser is 532 nm diode laser.

The MS-0 exhibit the characteristic Raman peaks of the 2H phase at 380 and 403 cm^{-1} corresponding to the in-plane E^1_{2g} and out-of-plane A_{1g} vibration modes, respectively. The Raman spectra of intercalated MoS_2 show three typical peaks of the distorted 1T' phase: the J_1 peak at 148 cm^{-1}, the J_2 peak at 236 cm^{-1}, and the J_3 peak at 336 cm^{-1}.[S1] The E_g vibration mode peak appears at 284 cm^{-1}. Therefore, the intercalated samples consisted of the 1T' phase.

Reference

(S1) D. Yang, S. J. Sandoval, W. M. R. Divigalpitiya, J. C. Irwin and R. F. Frindt, *Phys. Rev. B*, 1991, **43**, 12053-12056.

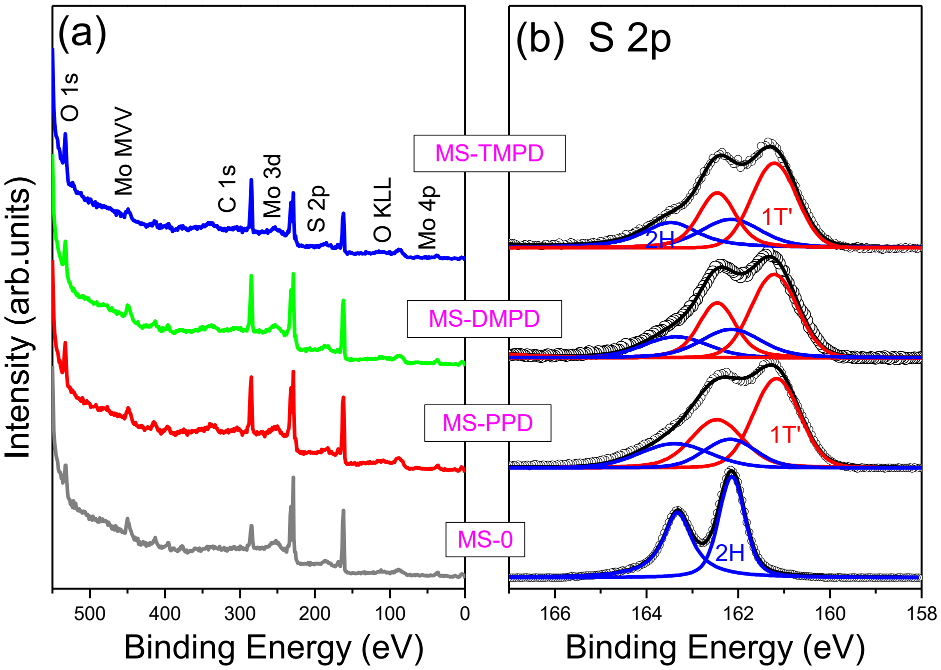

Fig. S5 (a) XPS survey scans of MS-0, MS-PPD, MS-DMPD, and MS-TMPD. The photon energy is 600 eV. (b) Fine-scan S 2p peak. The experimental data (open circles) are fitted by a Voigt function, and the sum of the resolved bands is represented by a black line.

(a) The C peak of MS-PPD, DMPD, and TMPD is larger than that of MS-0, due to the PD molecules. (b) The S $2p_{3/2}$ and S $2p_{1/2}$ peaks are separated by about 1.2 eV. The MS-0 sample shows peaks at 162.1 and 163.3 eV, which are 1.9 eV red-shifted with respect to the signal of neutral S (S^0) at 164.0 and 165.2 eV. They correspond to the S^{2-} anions bonded with the Mo cations in the 2H phase. For the intercalated MoS_2, the broad peak was resolved into four bands; two each for the 2H phase (blue) and the 1T' phase (red). The larger red-shift bands are assigned to those of electron-rich 1T' phase.

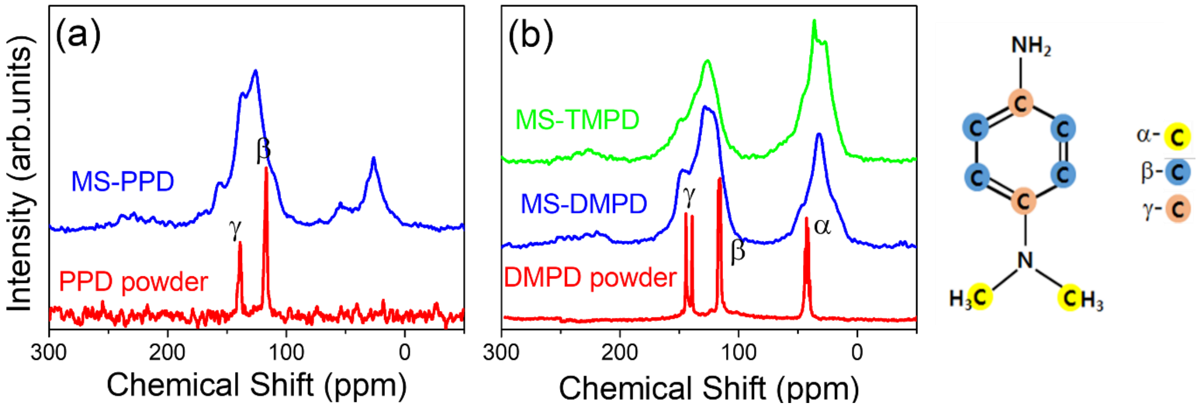

Fig. S6 Solid-state ^{13}C NMR spectra of (a) PPD powders and MS-PPD; (b) DMPD powders, MS-DMPD, and MS-TMPD. Schematic diagram of DMPD on the right shows the positions of α-C, β-C, and γ-C.

(a) The ^{13}C NMR spectrum of PPD powders show the β-C (C-C=C) and γ-C (>C-N) peaks at 116 and 139 ppm, respectively. MS-PPD shows peaks at 126 and 40 ppm with the area ratio of 1:0.3. The former peak originates from the β-C and γ-C atoms of the aromatic ring. The blue shift from that of PPD powders could indicate charge transfer to MoS$_2$. The peak at 26 ppm can be assigned to the carbons, which are generated by the decomposition of phenyl rings. The ratio of this C peak to the phenyl ring peak is 0.2. This decomposition of PD molecules could supply N atoms for the doping of MoS$_2$ during synthesis.

(b) DMPD powders show the α-C ((CH$_3$)$_2$-N-), β-C (C-C=C), and γ-C (> C-N) peaks at 44, 118, and 144 ppm, respectively. Both MS-DMPD and MS-TMPD show the β-C and γ-C peaks of aromatic ring at 123 and 146 ppm that are not separated. The ratio of the β-C and γ-C peaks is 2:1, indicating that intact PD molecules exist in MoS$_2$ after intercalation. The blue shift from that of the DMPD powders is also due to the charge transfer to MoS$_2$. Similar to MS-PPD, a peak at 30 ppm appears. The ratio of this C peak to the phenyl ring peak is 0.6 and 1.2 for MS-DMPD and MS-TMPD, respectively, which are higher than the values of 0.3 and 0.7 (expected value) for DMPD and TMPD molecules. The higher ratio is due to the C atoms that are generated from the dissociation of N(CH$_3$)$_2$ groups and phenyl rings. The decomposition could supply N atoms for the doping of MoS$_2$.

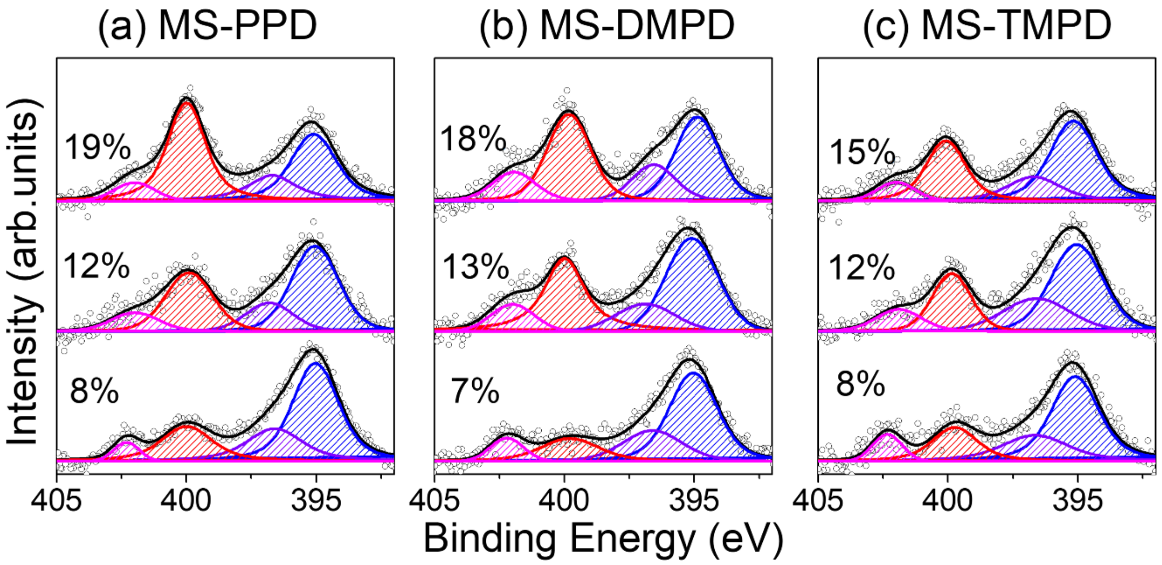

Fig. S7 Fine-scan of Mo $3p_{3/2}$ and N 1s peaks for (a) 8%, 12%, and 19%-intercalated PPD, (b) 7%, 13%, and 18%-intercalated DMPD, and (c) 8%, 12, and 15%-intercalated TMPD samples. The XPS data (open circles) are fitted by a Voigt function, and the sum of the resolved bands is represented by a black line.

The N 1s peak was resolved into three bands: N1 (402 eV), N2 (400 eV), and N3 (397 eV). The N1 and N2 bands are ascribed to the intercalated PDs; first one is positive charged form (N^+) and the second one is the neutral form. The N3 peak is assigned to the N atoms in N-Mo, respectively. The percentage concentration of intercalated PDs was estimated using the relative intensity (integrated area) of N 1s (N1 and N2 bands) and Mo 3d (Mo $3d_{5/2}$ and $3d_{3/2}$ peaks) signals. As the concentration of intercalated PD increases, the concentration of the cation form increases up to 5%, while that of the neutral form increases more significantly than that of the cation form (see summary in **Table 1** in the text). The N-doping concentration was calculated using the intensity ratio of N3 band and Mo 3*d* peak, and the value is about 10% for all samples.

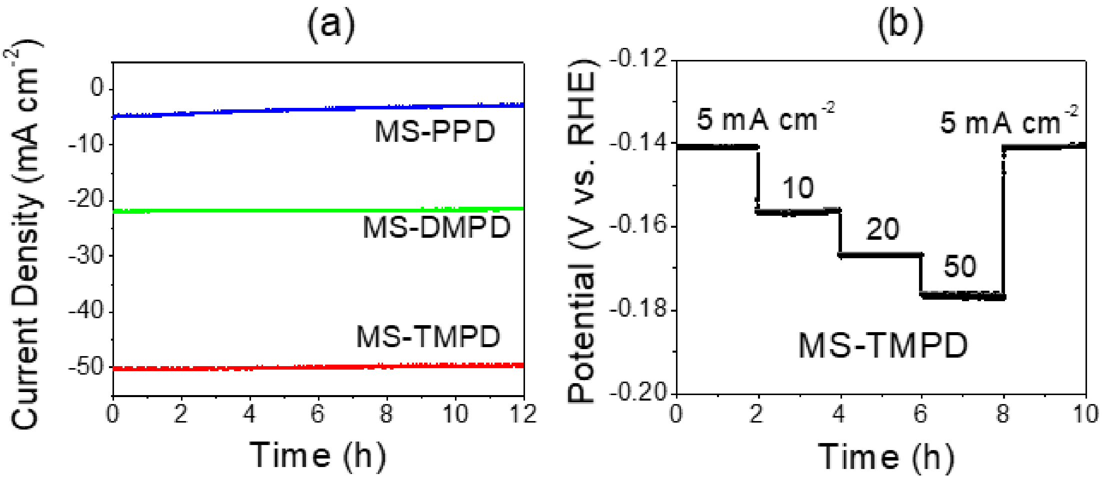

Fig. S8 (a) Chronoamperometric responses of MS-PPD, MS-DMPD, and MS-TMPD at 0.176 V for 12 h. (b) Chronopotentiometric response of MS-TMPD under multi-current-step condition from 5 to 50 mA cm^{-2}; 5 mA cm^{-2} at $\eta = 0.141$ V, 10 mA cm^{-2} at $\eta = 0.153$ V; 20 mA cm^{-2} at $\eta = 0.167$ V; 50 mA cm^{-2} at $\eta = 0.176$ V; 5 mA cm^{-2} at $\eta = 0.141$ V for each 2 h step.

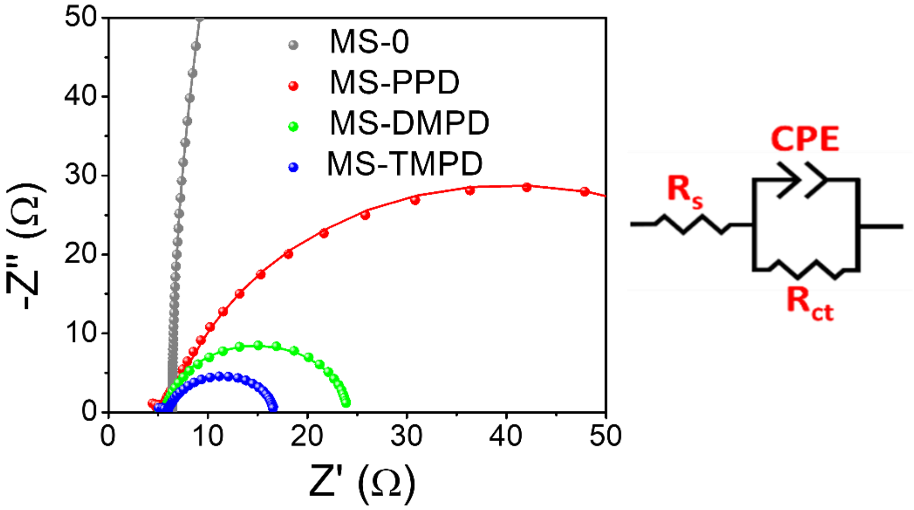

Fig. S9 Nyquist plots for EIS measurements from 100 kHz to 0.1 Hz at a representative potential of -0.15 V (vs. RHE). The modified Randles circuit for fitting is shown on the right.

Electrochemical impedance spectroscopy (EIS) measurements of the samples were performed using a 100 kHz–0.1 Hz frequency range and an amplitude of 10 mV at $\eta = 0.15$ V. In the high-frequency limit and under non-Faradaic conditions, the electrochemical system is approximated by the modified Randles circuit shown on the right of Figure S7, where R_s denotes the solution resistance, CPE is a constant-phase element related to the double-layer capacitance, and R_{ct} is the charge-transfer resistance from any residual Faradaic processes. A semicircle in the low-frequency region of the Nyquist plots represents the charge transfer process, with the diameter of the semicircle reflecting the charge-transfer resistance. The real (Z') and negative imaginary ($-Z''$) components of the impedance are plotted on the x and y axes, respectively. The simulation of the EIS spectra using an equivalent circuit model allowed us to determine the charge transfer resistance, R_{ct}, which is a key parameter for characterizing the catalyst-electrolyte charge transfer process. The fitting parameters are listed in **Table S2**.

The R_{ct} values follow an order consistent with the HER performance: MS-TMPD > MS-DMPD > MS-PPD > MS-0.

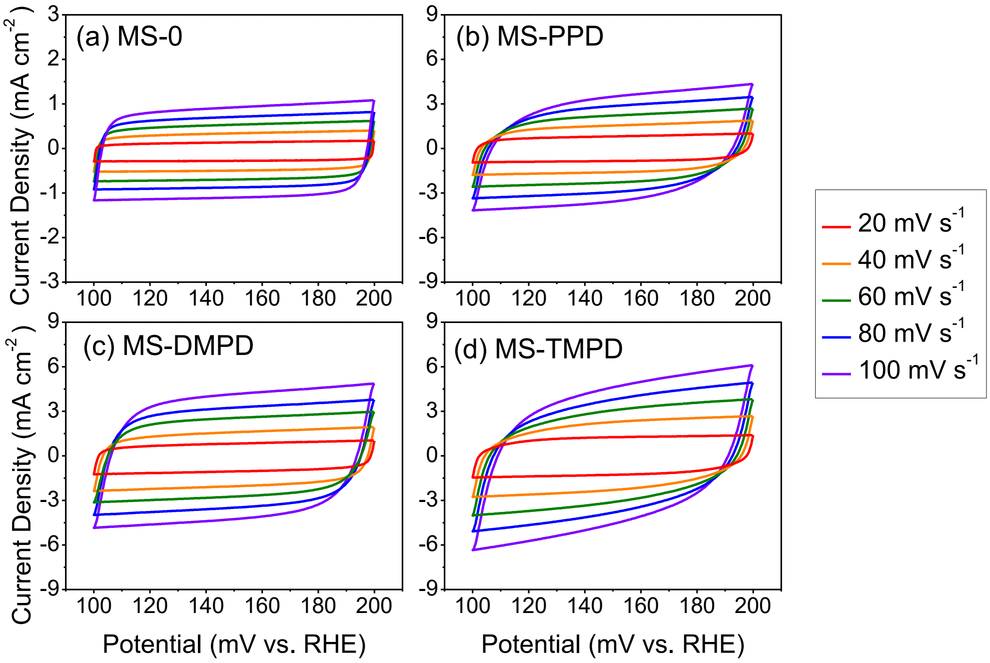

Fig. S10 Cyclic voltammograms of (a) MS-0, (b) MS-PPD, (c) MS-DMPD and (d) MS-TMPD in a non-Faradaic region (0.1-0.2 V vs. RHE), at 20-100 mV s^{-1} scan rates (with a step of 20 mV s^{-1}) and in 0.5 M H_2SO_4 solution.

Cyclic voltammograms were measured at 0.1-0.2 V, in a non-Faradaic region, using various scan rates. The double-layer capacitance (C_{dl}) was obtained as the slope of a linear fit of ΔJ vs. scan rate (20–100 mV s^{-1}), where ΔJ is the difference between the anodic charging and cathodic discharging currents.

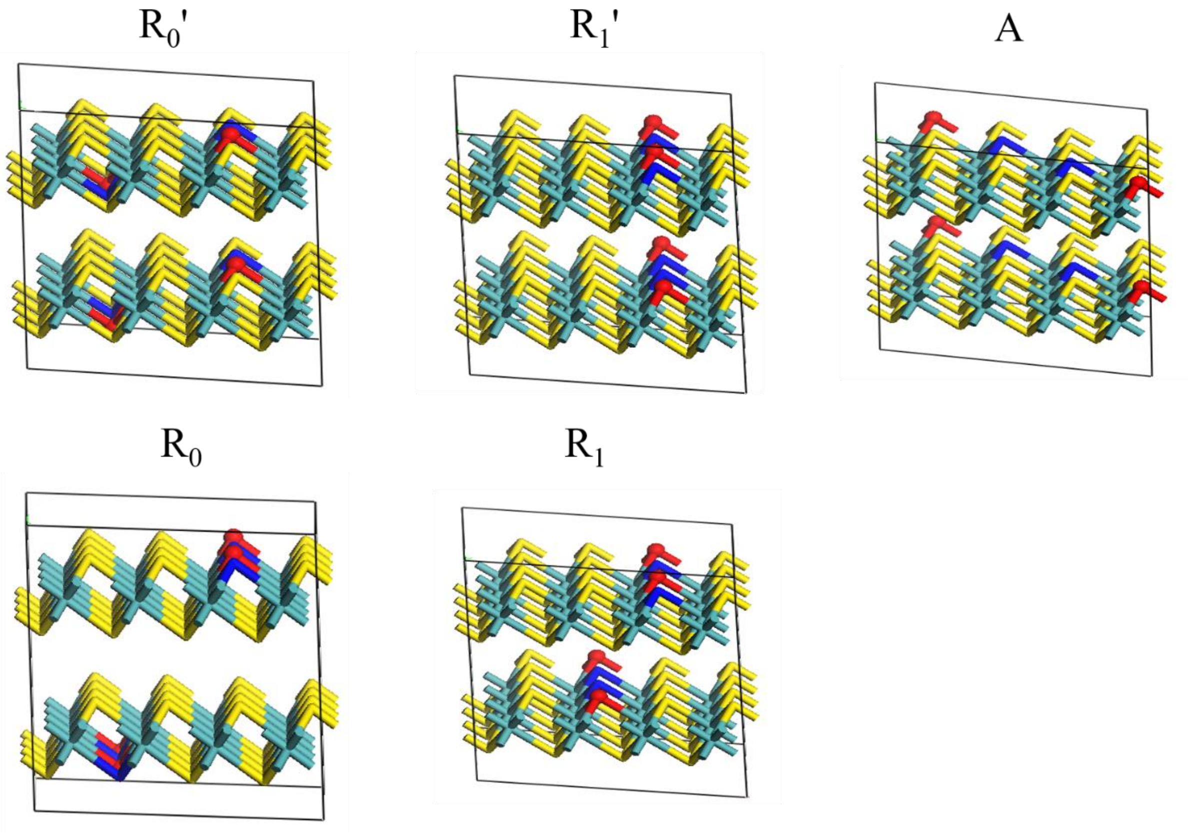

Fig. S11 Five configurations of $MoS_{2-2x}N_x$ ($x = 0.125$). Cyan, yellow, and blue sticks represent Mo, S, and N atoms, respectively, while red sphere and stick denote S vacancies.

In R_0', one-half of four S vacancies are located contiguously in the upper sublayer, and another half are located contiguously in the lower sublayer of the same MoS_2 layer. On the other hand, in R_0 all four S vacancies are located contiguously in one of the sublayers. R_1 and R_1' both have the S vacancies distributed in such a way that four of them are contiguous as in R_0. However, R_1' is different from R_1 in that the S vacancies are located in the same sublayer of different layers, instead of different sublayers. R_0' and R_1' are more stable than R_0 and R_1 by significant degrees, i.e., 0.87 and 1.02 eV, respectively. In the A configuration, the S vacancies are randomly scattered in a non-contiguous way.

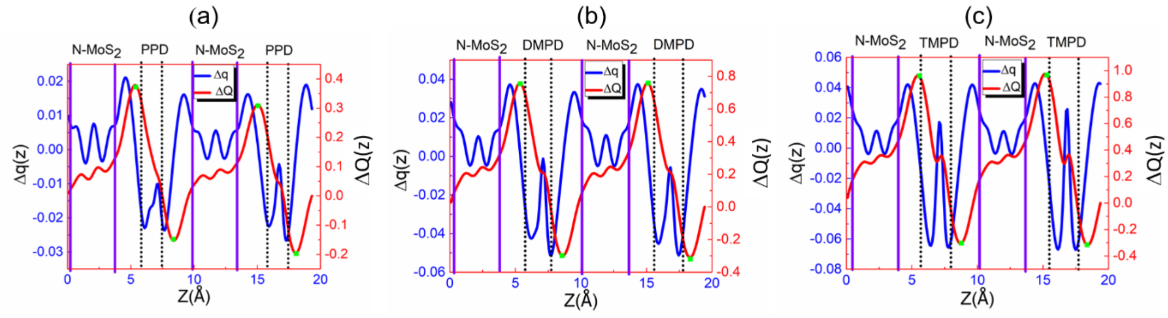

Fig. S12 $\Delta q(z)$ and $\Delta Q(z)$ versus z of (4 × 4)MoS_2-PD for (a) PPD, (b) DMPD, and (c) TMPD at 12.5%: z_{min} and z_{max} values corresponding to $Q_{min}(z)$ and $Q_{max}(z)$ are shown by filled squares (■), respectively.

Following our previous studies, the amount of the charge transfer was calculated [S1, S2]. The change in electron density (expressed in e $Å^{-3}$) along the c (= z) axis generated by the intercalation process was defined as $\Delta\rho(z) = \rho(z)\{MoS_2\text{-PD}\} - \rho(z)\{MoS_2\} - \rho(z)\{PD\}$, averaged over the *xy* plane in a supercell. The total electron density change (e) was defined as $\Delta q(z) = \Delta\rho(z)\Delta V$, where ΔV is the volume of a fine grid, *i.e.*, $\Delta V = V_{cell}/N_c$, in which V_{cell} is the total volume of the supercell and N_c is the number of fine grids. The thickness of each MoS_2 layer was defined on the basis of the z coordinates of the S atoms in the upper and lower sublayers (S_L and S_U), with $z(S_L) < z(S_U)$. The thickness of PD molecules was obtained from the minimum and maximum z coordinates of its atoms. The actual thickness might be larger than that obtained using this definition if the finite atomic size is taken into account. In addition, $Q(z)$, displayed on the right vertical axis represents the accumulated excess charge in the interval [0, z]: $Q(z)=\sum_{0}^{z'<z}\Delta q(z')$, i.e., the integration of charge difference $\Delta q(z')$ within $z' < z < c$.

The amount of charge transfer was defined as $\Delta Q = Q_{max} - Q_{min}$, where Q_{max} and Q_{min} correspond to the maximum and minimum charge values in the regions (marked by ■) adjacent to the MoS_2 layers and PD molecules, respectively. The ΔQ was 0.52e, 1.04e, and 1.26e for two PPD, DMPD, and TMPD molecules. The larger ΔQ value confirmed that a more significant charge transfer took place. The respective ΔQ^{PD} was calculated to be 0.26e, 0.52e, and 0.63e.

References:

(S1) I. H. Kwak, I. S. Kwon, H. G. Abbas, G. Jung, Y. Lee, T. T. Debela, S. J. Yoo, J. G. Kim, J. Park and H. S. Kang, *Nanoscale* 2018, **10**, 14726-14735

(S2) I. S. Kwon, I. H. Kwak, H. G. Abbas, G. Jung, Y. Lee, J. Park, S. J. Yoo, J. G. Kim and H. S. Kang, *Nanoscale* 2018, **10**, 11349-11356

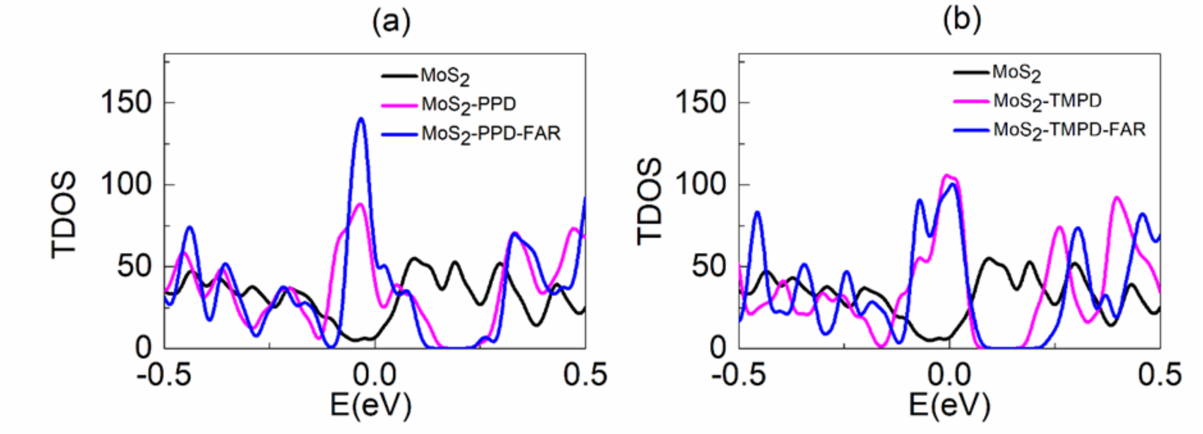

Fig. S13 TDOS of 1T' phase (a) (4×4) MoS_2, (4×4) MoS_2-PPD, and (4×4) MoS_2-PPD-FAR; (b) (4×4) MoS_2, (4×4) MoS_2-TMPD, and (4×4) MoS_2-TMPD-FAR.

In order to understand the TDOS of the 1T' phase (4×4) MoS_2-PD, we considered two other systems in the same phase: (4×4) MoS_2 and (4×4) MoS_2-PD-FAR. MoS_2 represents non-intercalated MoS_2 with the optimized *c* parameter. MoS_2-PD-FAR denotes an intercalated complex with *c* greater than the equilibrium value by 2.00 Å, so that there is only weak interaction between the MoS_2 layers and PD molecules. For a specific PD (= PPD or TMPD), comparison of the TDOS's of MoS_2 and MoS_2-PD-FAR shows that it increases significantly around the Fermi level by charge transfer from the PD molecules. Subsequent reduction of *c* to the equilibrium value introduces (1) a broadening of the TDOS due to the interaction of the MoS_2 with the PD and (2) an upward shift of the Fermi level due to another charge transfer. The TDOS is more enhanced in the MoS_2-TMPD than in the MoS_2-PPD.

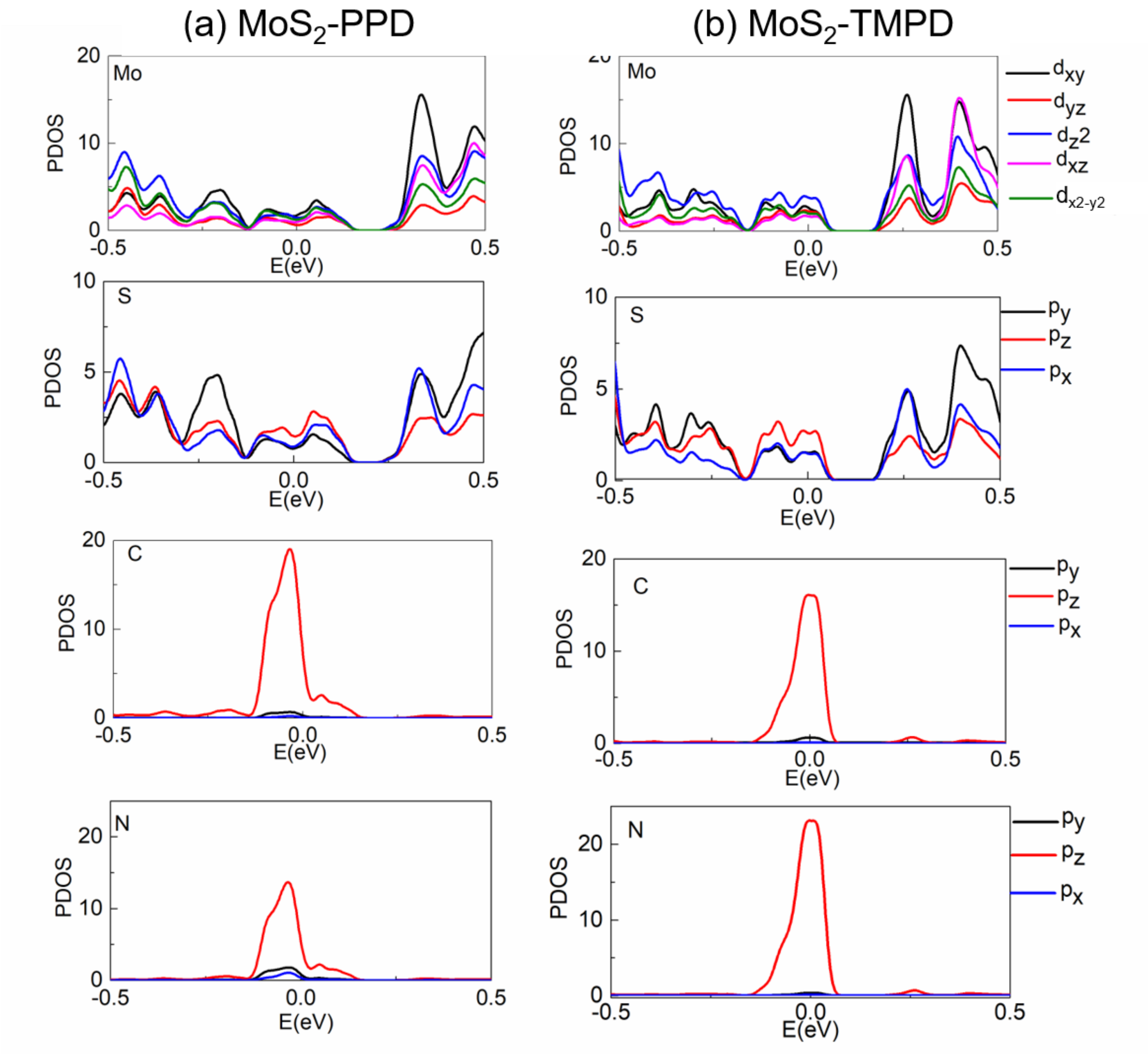

Fig. S14 Projected DOS (PDOS) of the (a) (4×4) MoS_2-PPD and (b) (4×4) MoS_2-TMPD onto various atomic orbitals.